



Visible-light induced $\text{CoMoO}_4@ \text{Bi}_2\text{MoO}_6$ heterojunction membrane with attractive photocatalytic property and high precision separation toward oil-in-water emulsion

Jingshuai Li¹, Yongli Sun¹, Luhong Zhang, Xiaoming Xiao, Na Yang, Longfei Zhang, Xiaodong Yang, Feifei Peng, Bin Jiang*

School of Chemical Engineering and Technology, Tianjin University, Tianjin 300072, People's Republic of China

ARTICLE INFO

Keywords:

Superhydrophilic membrane
Underwater superoleophobic
Visible-light photocatalysis
P-n heterojunction
Emulsion separation

ABSTRACT

The discharge of wastewater containing insoluble oils and water-soluble organic pollutants has caused severe water pollution and seriously threatened the sustainable development of human society. Membrane separation technology, on the basis of the size sieving and superwettability, can effectively remove insoluble oils from the wastewater, but still lacking the ability to degrade water-soluble pollutants. Herein, a novel heterojunction membrane with dual functionalities of superhydrophilicity and visible-light photocatalytic property was prepared by constructing hierarchical $\text{CoMoO}_4@ \text{Bi}_2\text{MoO}_6$ nanoarrays on Ni foam (NF@CM@BM) via a facile two-step hydrothermal process combined with calcination methods. Attributed to the synergistic application of photocatalysis, superhydrophilicity and underwater superoleophobicity, the membrane could simultaneously remove water-soluble organic pollutants and insoluble oils in wastewater efficiently. Completely driven by gravity, high oil/water separation efficiency of 99.67% could be achieved with the flux of $1449.12 \text{ L m}^{-2} \text{ h}^{-1}$. Besides, the formation of p-n heterojunction between p-type CoMoO_4 and n-type Bi_2MoO_6 greatly enhanced the photocatalytic ability to degrade Congo red with the efficiency of 97.1%. More importantly, the NF@CM@BM membrane exhibited excellent stability and recyclability, possessing great application potential in oily wastewater remediation. Therefore, we envision that this work will offer new insights into the design of wastewater remediation membranes.

1. Introduction

Owing to the rapid development of modern industry, frequent offshore oil leakage and the discharge of industrial wastewater containing organic pollutants make the issue of water resources increasingly tense, seriously threatening the ecological environment and human health [1–3]. Based on this, the effective treatment of oily wastewater has become an urgent issue to be solved. Although traditional technologies, such as centrifugation [4], chemical coagulation [5], air flotation [6] and microbial degradation [7] can achieve the separation of oil/water mixture to some extent, there are still problems of high operating cost, poor anti-pollution ability, low separation efficiency, and it is difficult to separate the miscible oil–water mixture, especially the emulsion with droplets size less than $20 \mu\text{m}$ [8–10]. Consequently, the efficient separation of emulsified oily wastewater is exceedingly

challenging and significant.

Analyzing from the theory of size-sieving effect, as long as the pore size of the separation membrane material is less than the droplet size of the emulsion, the emulsion will be intercepted on one side of the membrane material, thus realizing the separation of oil–water emulsion [11–13]. However, if the oil/water emulsion is separated only by aperture, the membrane will be easily contaminated with oil during the separation process, resulting in the decrease of its flux and separation efficiency. Hence, the wettability of the separation material is particularly important in the practical separation application of emulsified oily wastewater [14]. In recent years, inspired by natural phenomenon, membrane separation technology based on superwettability has attracted extensive attention of researchers because of its simple operation, low energy, high efficiency and low separation cost, and has been considered as one of the most potential oil–water separation

* Corresponding author at: School of Chemical Engineering and Technology, Tianjin University, Tianjin 300072, People's Republic of China.

E-mail address: binj@tju.edu.cn (B. Jiang).

¹ These authors contribute equally to this work.

technologies. Yin et al. [15] fabricated a bio-inspired anti-oil-fouling membrane decorated with urchin-like α -FeOOH particles via the layer-by-layer (LBL) self-assembly method, which exhibited superior superhydrophilicity/underwater superoleophobicity, high water-retention ability, and preferable anti-oil-fouling properties, thus endowing the membrane favorable separation performance for immiscible surfactant-stabilized oil-in-water emulsions. Zhang et al. [16] reported a $\text{Ti}_3\text{C}_2\text{T}_x$ MXene membrane by depositing ultrathin 2D $\text{Ti}_3\text{C}_2\text{T}_x$ MXene 2D nanosheets carbides onto porous polyvinylidene fluoride (PVDF) membranes by vacuum filtration, which displayed superior durability to the corrosive liquids such as acidic, alkaline and salty. Despite these superwettability based oil-water separation membranes have aroused enormous attention, they still cannot fulfill the purification of water-soluble organic pollutants in wastewater from textile and other industries [17]. In addition, the water-soluble dyes present in the oily wastewater will be absorbed on the membrane surface, which consequently deteriorate the flux and separation efficiency [18].

In the application of membrane technology based on superwettability, the introduction of catalytic reaction enables the membrane to interact with external stimuli such as electrical current, chemical activation and light, which may be used to degrade pollutants. As a promising green technology, semiconductor-based photocatalysis can effectively remove water-soluble organic pollutants from wastewater by converting solar energy [19–21]. Among numerous semiconductor materials, Bismuth-based materials with the valence band (VB) comprising the sp hybridization of O 2p and Bi 6s orbitals possess a relatively narrow band gap typically less than 3.0 eV, showing a strong visible light capture ability [22]. In particular, Bi_2MoO_6 , as an n-type semiconductor, is a promising photocatalyst with advantages of non-toxicity, low cost, high-stability and appropriate band gap of 2.5–2.8 eV [23–25]. However, the application of pure Bi_2MoO_6 is restricted due to the rapid recombination of photogenerated charge carriers and poor quantum yield, thus resulting in unsatisfied photocatalytic ability. To promote the photocatalytic performance of Bi_2MoO_6 , various technologies, such as semiconductor combination [26–28], element doping [29,30] and defect-introduction [31–33] were systematically explored over the past years. The construction of semiconductors heterojunction has been proved to be one of the most simple and effective methods to accelerate the separation of photogenerated carriers and suppress the recombination of charges by steering the charge kinetics, especially the p-n heterojunction. The coupling of p-type semiconductor and n-type semiconductor can further improve the separation and transfer of photo-induced carriers due to the formation of stronger internal electric field at the interface between the two types of semiconductors [34,35]. Meanwhile, according to our previous work, molybdate is a promising hydrophilic material that can be used for the preparation of superwetting membranes [36]. Therefore, the synergistic application of superwettability and photocatalytic oxidation to simultaneously remove insoluble oils and soluble dyes in wastewater is promising by designing Bi_2MoO_6 -based p-n heterojunction photocatalysts on suitable substrates.

Herein, we report a heterojunction membrane by constructing $\text{CoMoO}_4/\text{Bi}_2\text{MoO}_6$ p-n heterojunction nanoarrays on Ni foam via a facile two-step hydrothermal process combined with calcination methods (NF@CM@BM). Irregular Bi_2MoO_6 nanoparticles are uniformly dispersed on the CoMoO_4 nanosheets to form a rough hierarchical structure, which possesses favorable superhydrophilicity and underwater superoleophobicity, thus separating oil-in-water emulsions effectively. Besides, the NF@CM@BM membrane greatly enhances its photocatalytic capacity toward water-soluble pollutants since the formation of the p-n heterojunction not only enhances the absorption range and absorption intensity towards visible light, but also suppresses the recombination of photogenerated electrons and holes. More importantly, by virtue of attractive stability, recyclability and self-cleaning property, the as-prepared membrane maintains high separation efficiency and long lifespan. Therefore, the synergistic application of the superwettability and photocatalysis of the NF@CM@BM heterojunction

membrane can effectively remove water-soluble pollutants and insoluble oils in wastewater, which offers new insights for the design of porous membrane towards practical wastewater remediation.

2. Experimental

2.1. Materials

The Ni foam (pore size: 10 μm) was purchased from Guangjiayuan New Material Co. Ltd (Kunshan, China). Hydrochloric acid (HCl, 35%), Ethylene glycol (EG, 98%), Sodium molybdate dihydrate ($\text{Na}_2\text{MoO}_4 \cdot 2\text{H}_2\text{O}$, 98%) and Cobalt nitrate hexahydrate ($\text{Co}(\text{NO}_3)_2 \cdot 6\text{H}_2\text{O}$, AR) were obtained from Tianjin Heowns Biochemical Technology Co. Ltd (Tianjin, China). Bismuth nitrate pentahydrate ($\text{Bi}(\text{NO}_3)_3 \cdot 5\text{H}_2\text{O}$) and Congo red (CR) were from Tianjin Damao Chemical Reagent Co. Ltd (Tianjin, China). Deionized water was used in all experiments. All chemicals and reagents were used directly without further purification.

2.2. Preparation of CoMoO_4 nanosheet arrays on NF

The CoMoO_4 nanosheet arrays on Ni foam were synthesized by a facile hydrothermal method combined with a subsequent annealing process. Typically, a piece of pristine Ni foam (NF) with a size of $2.5 \times 2.5 \text{ cm}^2$ was sequentially cleaned with 3 M HCl solution, acetone, ethanol, deionized water via ultrasonic treatment for the remove of impurities on the surface. 2.5 mmol $\text{Na}_2\text{MoO}_4 \cdot 2\text{H}_2\text{O}$ and 2.5 mmol $\text{Co}(\text{NO}_3)_2 \cdot 6\text{H}_2\text{O}$ were dissolved in 50 ml deionized water under vigorous magnetic stirring for 30 min to form a wine-red solution. Then the cleaned Ni foam and reaction solution was transformed into a 100 ml Teflon-lined autoclave and maintained at 180 $^\circ\text{C}$ for 8 h. After cooling to room temperature, the obtained precursor was taken out and washed with ethanol and deionized water for several time before calcining at 350 $^\circ\text{C}$ for 2 h in air. Finally, the CoMoO_4 nanosheets coated Ni foam was obtained.

2.3. Synthesize of the NF@CM@BM heterojunction membrane

To synthesize the NF supported hierarchical $\text{CoMoO}_4/\text{Bi}_2\text{MoO}_6$ core-shell hybrid nanoarrays (NF@CM@BM), a second hydrothermal reaction was adopted to grow the micro Bi_2MoO_6 nanoparticles on the CoMoO_4 nanosheets. In detail, 1 mmol $\text{Na}_2\text{MoO}_4 \cdot 2\text{H}_2\text{O}$ and 2 mmol $\text{Bi}(\text{NO}_3)_3 \cdot 5\text{H}_2\text{O}$ were added to 20 ml EG under intense stirring with the assistance of ultrasound for 30 min. Afterwards, 40 ml ethanol was added into above solution and stirred for another 30 min. The obtained solution was poured into a 100 ml Teflon-lined autoclave, following heated at 160 $^\circ\text{C}$ for different time periods (4, 6, 8, 10, 12 and 14 h) to explore the growth process of Bi_2MoO_6 nanoparticles on the CoMoO_4 nanosheets. After cooling to room temperature, the NF supported hierarchical $\text{CoMoO}_4/\text{Bi}_2\text{MoO}_6$ core-shell nanoarrays were rinsed with deionized water for several times and further annealed at 350 $^\circ\text{C}$ for 2 h in air. Finally, the NF@CM@BM heterojunction membrane was obtained for later use and characterization.

The synthesis of Bi_2MoO_6 coated Ni foam was the same as that of NF@CM@BM except adding pristine Ni foam during the hydrothermal process. This sample was named as NF@BM.

2.4. Materials characterization

The X-ray photoelectron patterns (XRD) of all samples were analyzed using an XRD diffractometer (XRD, D8-Focus, AXS, Germany), with Cu $K\alpha$ radiation ($\lambda = 1.5406 \text{ \AA}$) in the 2θ range of 20–80 $^\circ$. The surface morphology of the NF supported hierarchical $\text{CoMoO}_4/\text{Bi}_2\text{MoO}_6$ core-shell nanoarrays and CoMoO_4 nanosheet arrays were performed on a field-emission scanning electron microscope (Regulus 8100, Japan), combined with energy dispersive spectrometer (EDS) to explore the

element distribution of the hierarchical CoMoO₄@Bi₂MoO₆ core-shell nanoarrays. The X-ray photoelectron spectroscopy (XPS, Thermo ESCALAB 250Xi, USA) was conducted on the measurement of the XPS survey to identify the composition of the surface. The UV-vis diffuse reflectance spectra (DRS) of the samples in the range of 200–800 nm were tested by a UV-vis spectrometer (Puxi, UV1901) with an integrating sphere using BaSO₄ as the reflectance standard. The ultraviolet-visible (UV-vis) absorption of the dye solutions were measured with a UV-vis spectrophotometer (UV-4802S, Unico, USA). All contact angles were tested by dropping the liquid droplet with 4–8 μl on the sample using an optical contact angle and an interface tension meter (SL200 KS, KINO, USA) at ambient temperature.

2.5. Oil-in-water emulsions separation

The oil-in-water emulsions separation experiment was implemented with a self-assemble device completely driven by gravity. The NF@CM@BM membrane with effective filtration area of 2.54 cm² was sandwiched between two flanges connected with glass tubes. A series of oils including petroleum ether, gasoline, kerosene, n-hexane and dichloromethane were selected to prepared oil-in-water emulsions. 10 g sample oils and 1000 ml deionized water were mixed under vigorous stirring using a homogenizer (Fluke homogenizer, FA25, 500 W) operated at 10000 rpm for 3 min to obtain oil-in-water emulsions. For each experiment, the heterojunction membrane was pre-wetted with water and 70 ml emulsions were poured into the filter-separation device. The separation flux was calculated by with the following Eq. (1).

$$F = \frac{V}{A \times t} \quad (1)$$

where V (L) represents the volume of permeate liquid, A (m²) is the effective filtration area of the heterojunction membrane and t (h) is the filtering time.

The separation efficiency of oil-in-water emulsion was calculated with following Eq. (2).

$$R = \left(1 - \frac{C_1}{C_0}\right) \times 100\% \quad (2)$$

where C_1 and C_0 represent the oil concentrations in the filtrate and feed, respectively, which are determined by the by a TOC analyzer (TOC, SHIMADZU, Japan).

2.6. Photocatalytic performance

The photocatalytic performance of NF@CM@BM membrane was evaluated by the photodegradation of Congo red (CR) under visible light. A 350 W Xe lamp connected with condensed circulating water was used as the light source. In a typical experiment, a piece of NF@CM@BM membrane with a size of 2.5 × 2.5 cm² was immersed in 40 ml CR solution (30 ppm) under stirring while a adsorption-desorption equilibrium was obtained under dark environment for 30 min before irradiation. It could be seen from Fig. S1 that as the adsorption time increased, the adsorption efficiency of the NF@CM@BM heterojunction membrane to CR solution increased gradually until it no longer changed significantly after 24 min, which indicated that 30 min was sufficient to reach the adsorption-desorption equilibrium. The degradation of the CR solution was monitored at an intervals time of 10 min and 5 ml mixture was taken out. Due to the inherent UV absorption characteristic of the organic dyes, the residual concentration of sample was estimated with a UV-vis spectrophotometer. The degradation efficiency $\eta_{\text{Degradation}}$ (%) was calculated by Eq. (3).

$$\eta_{\text{Degradation}} = \left(\frac{C_0 - C}{C_0}\right) \times 100\% \quad (3)$$

where C_0 and C are the dye concentration before irradiation and after

irradiation at different times, respectively.

3. Results and discussion

3.1. Design and characterization of the heterojunction membrane

Porous materials with special superwettability have been extensively employed in oily sewage separation. However, for oily wastewater with complex composition, although these materials are effective in removing oil from the wastewater, they still lack the ability to purify water-soluble pollutants. Based on this, the NF@CM@BM membrane coupling special wettability and photocatalysis was designed, which could remove insoluble oils and soluble dyes simultaneously from wastewater. In this work, Ni foam with advantages of porosity, high strength and toughness was selected as the substrate. As illustrated in Fig. 1, the CoMoO₄ precursor (CoMoO₄·xH₂O) stemmed from the combination of Co²⁺ and MoO₄²⁻ ions was prepared via the first-step facile hydrothermal process [37]. After further calcination, Ni foam supported CoMoO₄ nanosheet arrays would be obtained. Subsequently, Bi₂MoO₆ nanoparticles were uniformly grown on the CoMoO₄ nanosheets via nucleation and crystal growth under a second-step hydrothermal reaction followed by the annealing process.

The morphologies and nanostructures of CoMoO₄ and hierarchical CoMoO₄@Bi₂MoO₆ core-shell nanoarrays on Ni foam with different magnifications were analyzed by SEM. As shown in Fig. 2a, it could be clearly observed that the interconnected CoMoO₄ nanosheets with an opened-up network were uniformly distributed on the Ni foam, forming a rough CoMoO₄ film. The high magnification SEM image displayed that the thickness of CoMoO₄ nanosheets was about 28.6 nm and there was abundant open spaces between nanosheets with better surface accessibility, which was contributed to the growth of Bi₂MoO₆ nanolayer (Fig. 2b). It's undoubtedly that the 3D nano-substrate formed by the growth of nanosheets on Ni foam increased the roughness of Bi₂MoO₆. After the growth of Bi₂MoO₆ nanoparticles, the outer surfaces of CoMoO₄ nanosheet nanoarrays became very rough (Fig. 2c). As shown in Fig. 2d, the irregular Bi₂MoO₆ nanoparticles were uniformly distributed on the surface of CoMoO₄ nanosheets, confirming the successful construction of CoMoO₄@Bi₂MoO₆ core-shell nanoarrays on Ni foam. In addition, the EDS mappings were performed to analyze the element composition and distribution of NF@CM@BM heterojunction membrane. From the Fig. 2e-i, the elements of Mo, Co, O and Bi were homogeneously distributed, further identifying the component of hierarchical nanoarrays and content of each element.

To investigate the grow process of Bi₂MoO₆ nanoparticles on the CoMoO₄ nanosheets, a series of hydrothermal experiments were carried out under different reaction periods (4, 6, 8, 10, 12 and 14 h). The SEM images of Bi₂MoO₆ at different times were shown in Fig. S2. As discussed above, there were nothing on the CoMoO₄ nanosheets before the the second hydrothermal reaction. Nevertheless, it could be seen from Fig. S2a that the surface of nanosheets was covered with tiny nanocrystals after 4 h reaction in a Teflon-lined autoclave. With the increase of reaction time, there was no obvious change of the morphology of nanocrystals until the reaction time of 8 h (Fig. S2b, c). In this period, it was a process of dissolution and recrystallization in the solution that the nanocrystals were gradually dissolved into Bi₂O₂²⁺ and MoO₄²⁻ ions and turned into small nanoparticles [38]. As the reaction proceeded, the Bi₂MoO₆ nanoparticles gradually increased in size (Fig. S2d) and eventually grew into an irregular particle shape (Fig. S2e), evenly distributing on the surface of the nanosheet, which was due to high intrinsic anisotropic properties of Bi₂MoO₆. When the reaction time was increased to 14 h, the Bi₂MoO₆ film on the nanosheet arrays became irregular and thicker due to the accumulation of redundant crystals (Fig. S2f). In this system, driven by electrostatic interactions and coordination, irregular Bi₂MoO₆ nanoparticles were anchored on the nanosheets surface, thus forming hierarchical CoMoO₄@Bi₂MoO₆ core-shell nanoarrays with good morphology,



Fig. 1. Schematic illustration of the designed process of NF@CM@BM heterojunction membrane.

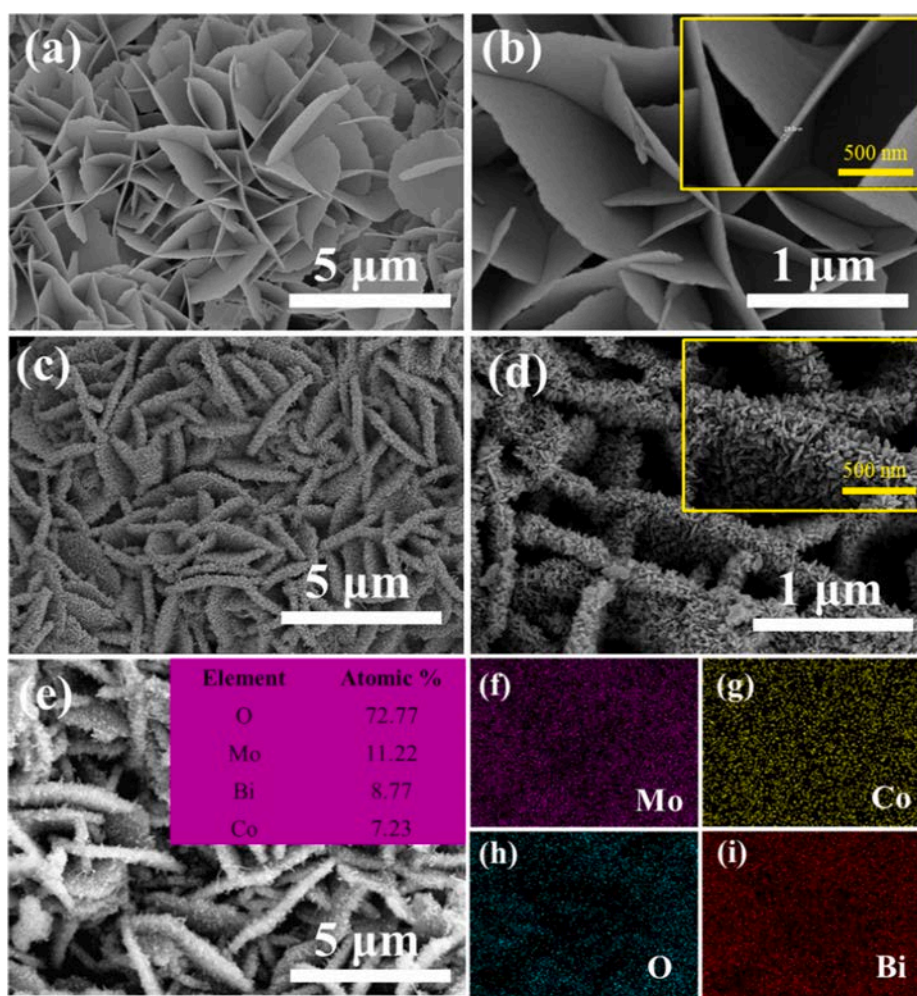


Fig. 2. SEM image of (a, b) CoMoO₄ nanosheets on NF, and (c, d) NF supported hierarchical CoMoO₄@Bi₂MoO₆ core-shell nanoarrays. (e) Selected area electron diffraction patterns of sample and (f-i) EDS mapping images of the NF@CM@BM heterojunction membrane.

which possessed strong interaction between CoMoO₄ and Bi₂MoO₆ nanoparticles.

The crystalline structure and composition of all samples were analyzed by X-ray diffraction (XRD) patterns. As displayed in Fig. 3a, diffraction peaks on the purple line observed at 2θ of 23.37°, 26.54°, 28.50°, 32.11° and 38.86° were assigned to the (021), (002), (-311),

(-131) and (040) crystallographic planes of monoclinic phase CoMoO₄ (JCPDS 21-0868), indicating the successful fabrication of CoMoO₄ nanosheets after the first process [39,40]. On the red line, the diffraction peaks of pure Bi₂MoO₆ at 28.27°, 32.52°, 46.74°, 55.46° and 58.53° indexed to the (131), (200), (202), (331) and (262) planes could be matched well with the standard card of orthorhombic phase Bi₂MoO₆

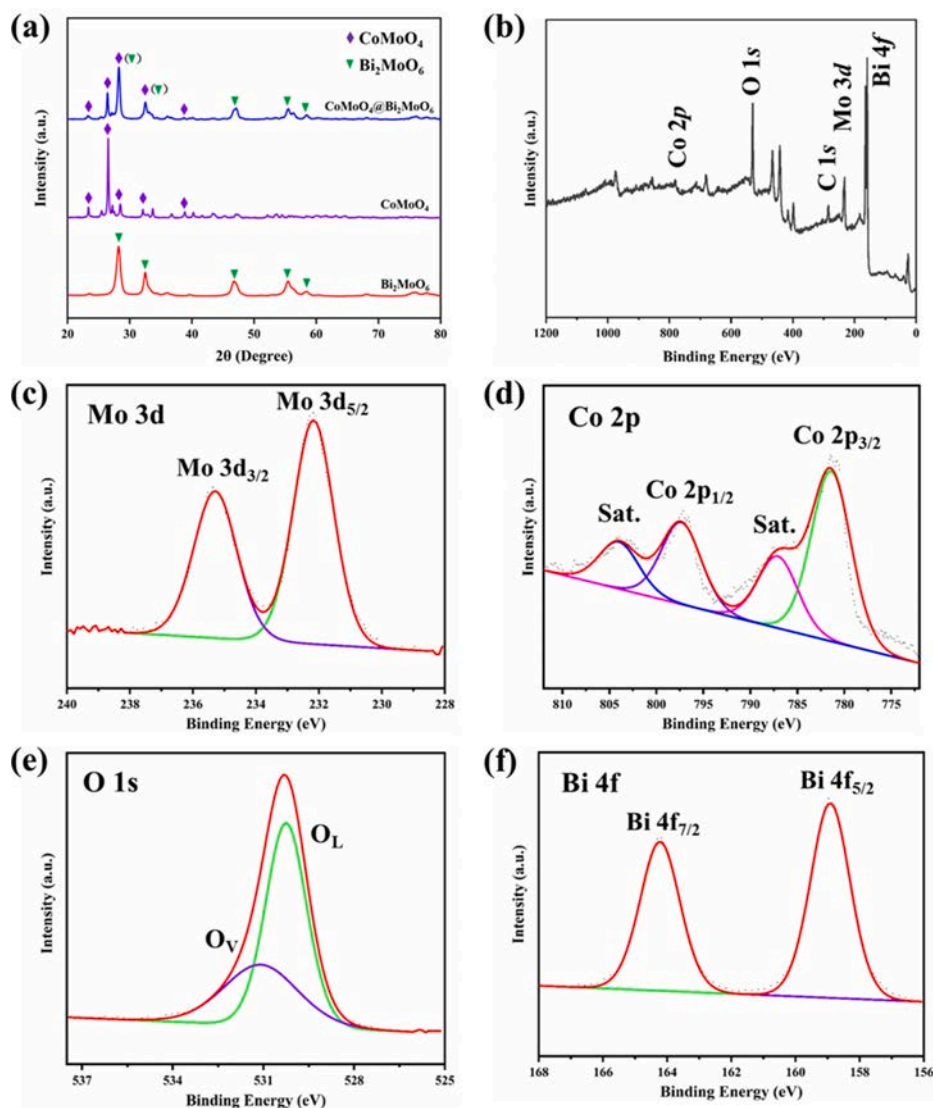


Fig. 3. (a) XRD patterns of samples CM, BM and NF@CM@BM, (b) Full-scale XPS survey spectrum of NF@CM@BM and high-resolution XPS spectra of (c) Mo 3d, (d) Co 2p, (e) O1s and (f) Bi 4f.

(JCPDS 21-0102) [41]. It could be observed that diffraction peaks of CoMoO_4 and Bi_2MoO_6 co-existed on the blue line after the growth of Bi_2MoO_6 nanoparticles on the CoMoO_4 nanosheets and no extra peaks were found, indicating the successfully construction of hierarchical $\text{CoMoO}_4@/\text{Bi}_2\text{MoO}_6$ heterojunction nanoarrays. Fig. S3 showed the local enlarged XRD patterns of all samples from the 2θ values 25° to 30° . It was worth noting that the diffraction peaks of $\text{CoMoO}_4@/\text{Bi}_2\text{MoO}_6$ slightly shifted to a lower 2θ value compared to the pure CoMoO_4 , which might be attributed to the lattice expansion caused by the substitution of Bi^{3+} (108 \AA) with a larger ionic radius for Co^{2+} (74 \AA) a smaller ionic radius during the hydrothermal reaction and calcination processes [42,43].

The chemical composition and valence states of the NF@CM@BM heterojunction membrane were investigated by XPS. As displayed in Fig. 3b, there were four elements of Mo, Co, O and Bi in the full-scale XPS survey spectrum aside from the C element using for binding energy correction of each element, which was consistent with the result of EDS analysis. In the high-resolution Mo 3d spectrum (Fig. 3c), two well-fitted peaks located at 232.17 eV and 235.29 eV with the separation of spin energy 3.06 eV was ascribed to Mo 3d_{3/2} and Mo 3d_{5/2} of Mo^{6+} respectively. As shown in Fig. 3d, the Co 2p spectrum split into four main peaks at the bind energy of 780.7 eV, 785.4 eV, 796.6 eV and

804.8 eV, respectively. The fitted peaks located at 780.7 eV and 796.6 eV accompanied two satellite peaks were assigned to Co 2p_{1/2} and Co 2p_{3/2}, indicating the existence of Co^{2+} . In the high-resolution O 1s spectrum (Fig. 3e), it could be observed that two peaks exhibiting at the binding energy of 530.25 eV and 531.11 eV were corresponded to the lattice oxygen and oxygen vacancies, respectively. In Fig. 3f, the high-resolution Bi 4f spectrum of NF@CM@BM was deconvoluted into two major peaks at the binding energy of 158.9 eV and 164.2 eV related to the Bi 4f_{7/2} and Bi 4f_{5/2}, indicating that the elemental Bi existed as Bi^{3+} in molybdates. Therefore, the above results of XPS analysis clearly corroborated the composition and valence states of the elements of Ni foam supported hierarchical $\text{CoMoO}_4@/\text{Bi}_2\text{MoO}_6$.

The optical absorption properties of CoMoO_4 , Bi_2MoO_6 and NF@CM@BM were investigated by UV–vis diffuse reflectance spectrometer (DRS). As shown in Fig. 4a, the absorption band edges of p-type CoMoO_4 and n-type Bi_2MoO_6 were located at around 680 nm and 460 nm, respectively, which was consistent with reported literatures [23,44]. It was noting that there was a hump in the region of 500–600 nm of the the absorption peak of CoMoO_4 , which was attributed to the fluctuation caused by the high-spin d-d transition mode of Co^{2+} [45,46]. Compared with pure Bi_2MoO_6 , the absorption band edge of NF@CM@BM of visible light was extended to 650 nm and there was a

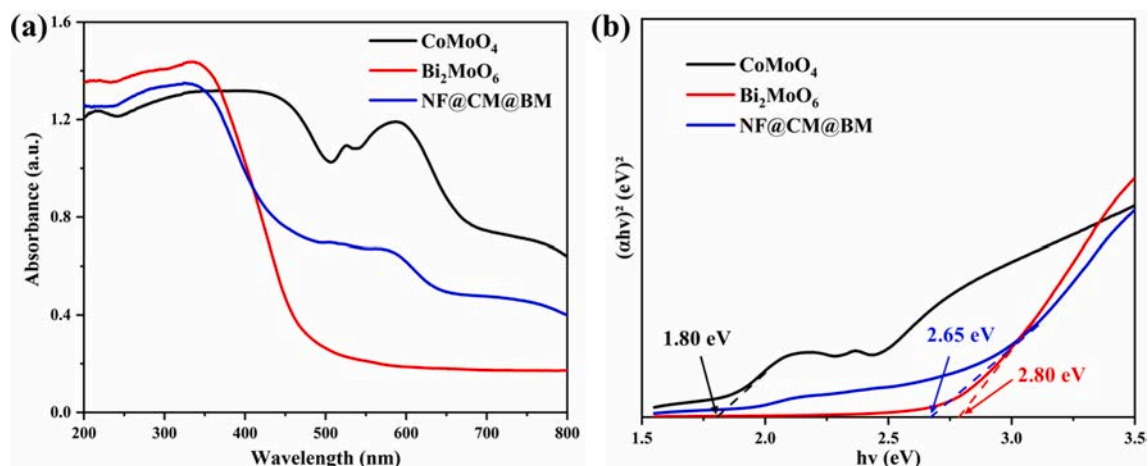


Fig. 4. (a) The UV-vis absorption spectra of CoMoO₄, Bi₂MoO₆ and NF@CM@BM. (b) The corresponding band gaps of the samples.

distinct absorption peak in the region of 500–650 nm, indicating that the visible light absorption capacity was significantly enhanced after the construction of the hierarchical CoMoO₄@Bi₂MoO₆ p-n heterojunction on Ni foam. Due to the increase in the absorption range and absorption intensity to visible light, the NF@CM@BM heterojunction membrane could generate more photogenerated electron-hole pairs under the irradiation of visible light. In addition, the corresponding band gap energy (E_g) of the samples were calculated by the Kubelka-Munk equation as following Eq. (4).

$$\alpha hv = A(hv - E_g)^{n/2} \quad (4)$$

where α , hv , E_g , and A are the absorption coefficient, photonic energy, band gap, and a constant, respectively. The value of n is 1 determined by the type of semiconductor. The band gaps of CoMoO₄, Bi₂MoO₆ and NF@CM@BM were estimated to be 1.80, 2.80 and 2.65 eV, respectively (Shown in Fig. 4b). These results were attributed to the formation of CoMoO₄@Bi₂MoO₆ p-n heterojunction, which significantly improved the responsiveness to visible light, thus possibly enhancing the

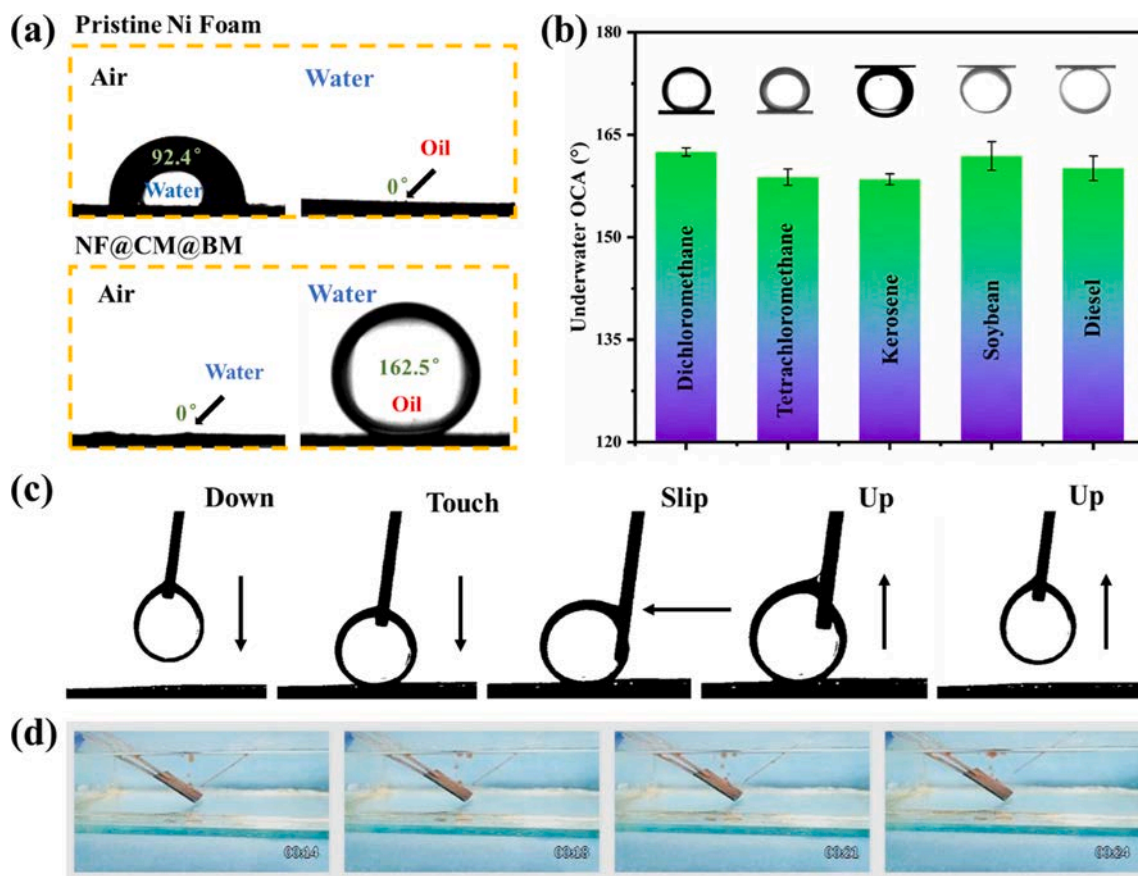


Fig. 5. (a) The WCA and underwater OCA of pristine Ni foam and NF@CM@BM heterojunction membrane. (b) The underwater OCA of different oil droplets on the NF@CM@BM heterojunction membrane. (c) Underwater oil adhesion test of NF@CM@BM heterojunction membrane. (d) Oil dyed with oil red was injected on the surface of the as-prepared membrane.

photocatalytic performance of the NF@CM@BM membrane. To investigate the effect of hierarchical CoMoO₄@Bi₂MoO₆ nanoarrays on the specific surface area of Ni foam, the Brunauer-Emmett-Teller (BET) analysis was carried out. As shown in Fig. S4, the specific surface area of NF@CM@BM membrane was 2.7 times than that of the original Ni foam, which was conducive to the full contact of dye with NF@CM@BM membrane, thereby promoting the photocatalytic degradation of dye.

3.2. Wettability of the NF@CM@BM membrane

The special wettability of the material surface is one of the prerequisites for the separation of oil/water mixture, which is influenced by their surface roughness and chemical composition. To explore the surface wetting behavior of pristine Ni foam and NF@CM@BM, the water contact angle (WCA) and underwater oil contact angle (OCA) were measured. As shown in Fig. 5a, the pristine Ni foam possessed a WCA of 92.4° in air and an underwater OCA of 0° in water, indicating that the wettability of Ni foam was not suitable for the separation of oil/water mixture. According to our previous work, molybdate is a potential hydrophilic material with selective wetting properties. After the construction of hierarchical CoMoO₄@Bi₂MoO₆ core-shell nanoarrays composed of hydrophilic constituent, the WCA in air was decreased to 0° from 92.4°, which demonstrated the favorable superhydrophilicity of the heterojunction membrane. In addition, the oil droplet in water on the surface of the NF@CM@BM heterojunction membrane was almost completely spherical, with a contact angle of 162.5°. In addition, the as-prepared membrane also performed splendid underwater ultra-oleophobicity for other oils, such as dichloromethane, tetrachloromethane, kerosene, soybean oil and diesel, and the corresponding underwater OCA were 162.5°, 158.8°, 158.5°, 161.9° and 160.1°, respectively (Fig. 5b). Moreover, the anti-oil-adhesion ability of NF@CM@BM was further characterized by the squeeze-lift experiment of oil droplet as shown in Fig. 5c. After being squeezed by the needle, the oil droplet sufficiently contacted with the surface of membrane and slid to the side without significant deformation. Subsequently, it was lifted up easily without leaving any oil on the surface. When injecting the oil bundle dyed with oil red into the membrane surface with a syringe underwater, the oil immediately bounced from the membrane surface and floated to the water without adhesion (Fig. 5d). The above experiments indicated that the NF@CM@BM membrane possessed favorable anti-oil-adhesion performance in water. Due to the difference of surface tension between oil phase and water phase, water completely wetted the surface of the NF@CM@BM and was trapped in the multi-level nanostructure to form a layer of water molecules with strong oil repellency, significantly reducing the area of oil-solid interface. This wetting behavior can be described by the Cassie-Baxter model with following Eq. (5):

$$\cos\theta_{OCA}^* = f\cos\theta_{OCA} + f - 1 \quad (5)$$

where the θ_{OCA}^* and θ_{OCA} are the underwater OCA of NF@CM@BM and pristine Ni foam, respectively and f represents the area fraction of the as-prepared heterojunction membrane. In this work, take dichloromethane as an example, the θ_{OCA}^* and θ_{OCA} are 162.5° and 0°, respectively. The value of f is calculated by Cassie-Baxter to be 0.023, which means that 97.7% of contact area is oil/water interface. Therefore, it is not difficult to understand why the NF@CM@BM possesses splendid underwater superoleophobicity, which is contributed to the enhancement of anti-fouling.

3.3. Oil-in-water emulsions separation

The special wetting behavior of the NF@CM@BM membrane makes it possible to separate oil-in-water emulsions. To explore the separation capability of the as-prepared membrane, a series of separation experiments for gasoline-in-water emulsion, kerosene-in-water emulsion, n-

hexane-in-water emulsion, petroleum ether-in-water emulsion and dichloromethane-in-water emulsion were conducted. Fig. S5 displayed the separation device before and after separation, respectively, which was completely driven by gravity. Due to the favorable superhydrophilicity and strong oil repellency of the pre-wetting NF@CM@BM membrane, after pouring oil-water emulsions into the separation device, water penetrated through the membrane while the oil was blocked above the membrane (Video S1). From the filtrate collected in the beaker, it could be observed that the milky white emulsion became clear, indicating the successful separation of oil-in-water emulsion. Fig. 6a-d illustrated the results of DLS analysis and optical microscope of different types of oil-in-water emulsions. Although the particle size distribution of different types of oils with the same preparation method was inconsistent, there were almost no oil droplets in the filtrates compared with the feeds.

To further explore the separation performance of the NF@CM@BM membrane, the separation efficiency of oil-in-water emulsions were calculated. As shown in Fig. 7, NF@CM@BM heterojunction membrane exhibited high separation efficiencies for five different oil-in-water emulsions, all of which were greater than 98 %, especially the separation efficiency of dichloromethane-in-water emulsion was as high as 99.67%. The penetrate flux of five kinds of oil-in-water emulsions were 1300.85, 1246.92, 1044.72, 909.92 and 1449.12 L m⁻²h⁻¹, respectively. From above results, the favorable separation performance was obtained for various oil-in-water emulsions, which meant the promising of NF@CM@BM membrane in oil/water separation. It was noting that the penetrate fluxes varied for different types of oil-in-water emulsions due to the comprehensive effect of viscosity, density as well as the oil droplets concentrations [36,47,48]. In addition to the selective wettability of the membrane, the distribution of the oil droplets is also an important factor affecting the separation efficiency of the oil-in-water emulsions. The variation of separation efficiency was exactly opposite to the distribution of the oil droplets shown in DLS analysis and optical micrograph, which further indicated the main dominance of the size-sieving effect.

The construction of hierarchical CoMoO₄@Bi₂MoO₆ core-shell nanoarrays on NF endowed the membrane with favorable superhydrophilicity and underwater superoleophobicity. As illustrated in Fig. 8, a plausible mechanism of NF@CM@BM heterojunction membrane for the separation of emulsions was analyzed. As the analysis of membrane wetting behavior, a stable hydration shell with strong repellency to oil was formed on the surface of the multi-level nanostructure, which provided an upward intrusion pressure ($\Delta P > 0$) to block the oil phase from penetrating through the membrane, while the intrusion pressure of water was downward allowing water to penetrate (Fig. 8a) [49]. In Fig. 8b, the oil droplet driven by gravity moved downwards to the bottom and the concentration of oil kept increasing with the decrease of water content [50]. Consequently, due to the enhancement of coalescence effect, the size of oil droplets increased significantly and floated above the water phase [51]. Finally, all the water phase passed through the NF@CM@BM heterojunction membrane, while the oil phase was blocked above due to the strong repellency to oil, thus achieving the separation of oil-in-water emulsions.

3.4. Photocatalytic performance of the NF@CM@BM heterojunction membrane

Due to the composition of hydrophilic molybdate and the rough structure formed by hierarchical CoMoO₄@Bi₂MoO₆ nanoarrays, the NF@CM@BM heterojunction membrane separates oil-in-water emulsions with high precision, effectively removing insoluble oil. However, the adsorption of dyes on the surface of NF@CM@BM heterojunction membrane would cause the separation performance to decrease. As shown in Fig. S6, compared with the NF@CM@BM membrane before the dye absorption, the separation efficiency for oil-water emulsion reduced from the initial 99.67% to 99.34%, and the corresponding

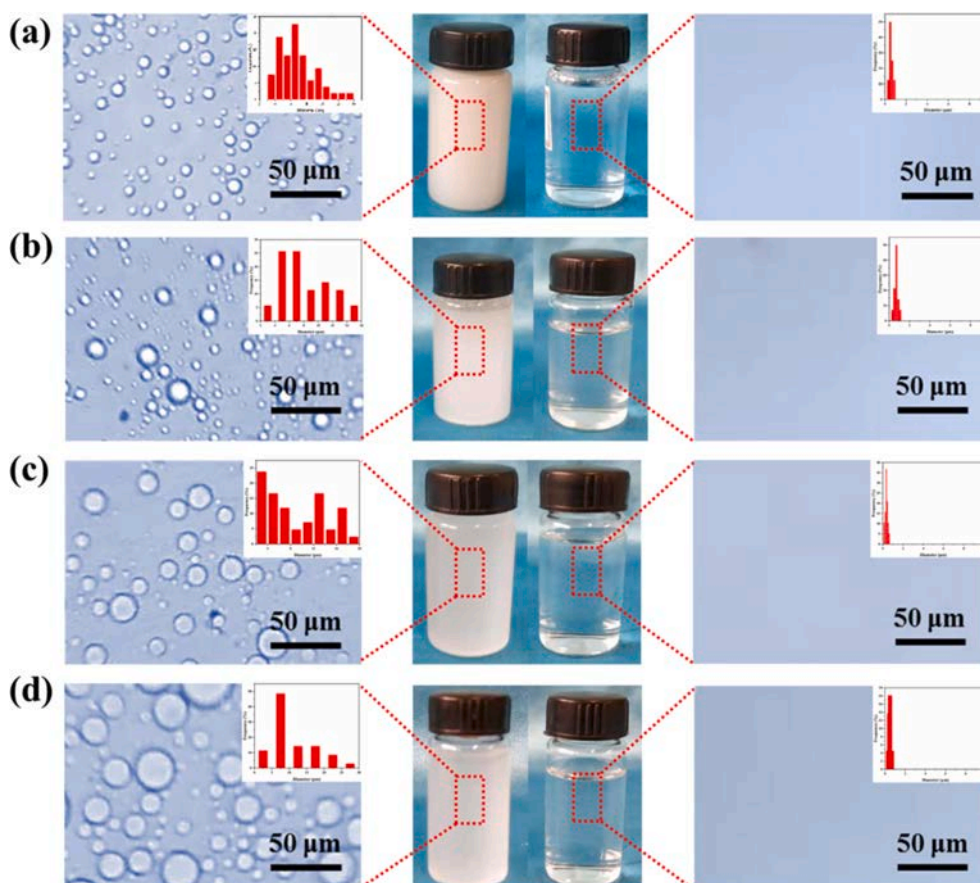


Fig. 6. Droplet distributions of various oil-in-water emulsions: (a) gasoline-in-water emulsion, (b) kerosene-in-water emulsion, (c) hexane-in-water emulsion and (d) petroleum ether-in-water emulsion.

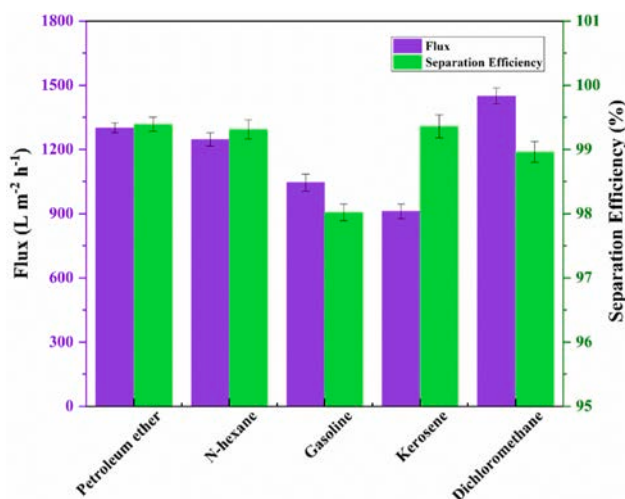


Fig. 7. Separation efficiency and permeation flux of various oil-in-water emulsions.

contact angle was also reduced from the initial 162.5° to 158.9°. Fortunately, the result of optical absorption property indicated that the formation of p-n heterojunction was contributed to the enhancement of absorption range and absorption intensity to visible light, which provided the possibility for the photocatalytic degradation of water-soluble pollutants. The photocatalytic performance of NF@CM@BM heterojunction membrane was further evaluated by the degradation of CR solution (30 ppm) under visible-light irradiation and the concentration

of CR solution at different times was calculated with a standard curve (Fig. S7). As shown in Fig. 9a, as the increase of irradiation time, the absorbance intensity of the CR solution diminished gradually, and it could be observed that the solution turned from the initial yellowish red to basically colorless after 60 min of visible light irradiation, indicating the successful degradation of CR. First of all, a controlled trial was conducted with Ni foam, the self-degradation rate of CR was less than 8%, which was basically negligible (Fig. 9b). After 60 min irradiation, the degradation efficiencies of NF@CM, NF@BM and NF@CM@BM were 63.9%, 77.10% and 97.1%, respectively. This difference was ascribed to the design of p-n CoMoO₄@Bi₂MoO₆ heterojunction, which greatly enhanced the photocatalytic ability due to the formation of a stronger internal electric field at the interface of CoMoO₄ and Bi₂MoO₆. Furthermore, to quantitatively investigate the degradation behavior of CR, a simplified Langmuir-Hinshelwood model was used to fit the kinetic curve for photocatalytic degradation as following Eq. (6).

$$\ln(C_0/C) = kt \quad (6)$$

where C_0 , C and k are the initial concentration, the concentration at time t and first-order kinetic constants, respectively. As illustrated in Fig. 9c, the reaction rate constant k of NF@CM@BM, NF@BM, NF and NF@CM were 0.05901, 0.02236, 0.01726 and 0.00134 min⁻¹, respectively. It was noting that the k value of the NF@CM@BM membrane was 2.64, 3.41 and 44.04 times higher than NF@BM, NF@CM and pristine Ni foam, indicating the excellent photocatalytic degradation rate of the membrane, as well as the construction of p-n heterojunction was an effective approach to enhance the photocatalytic ability of photocatalyst. Compared with other photocatalytic materials (Shown in Table S1), the NF@CM@BM heterojunction membrane possessed favorable photocatalytic performance and also improved the utilization

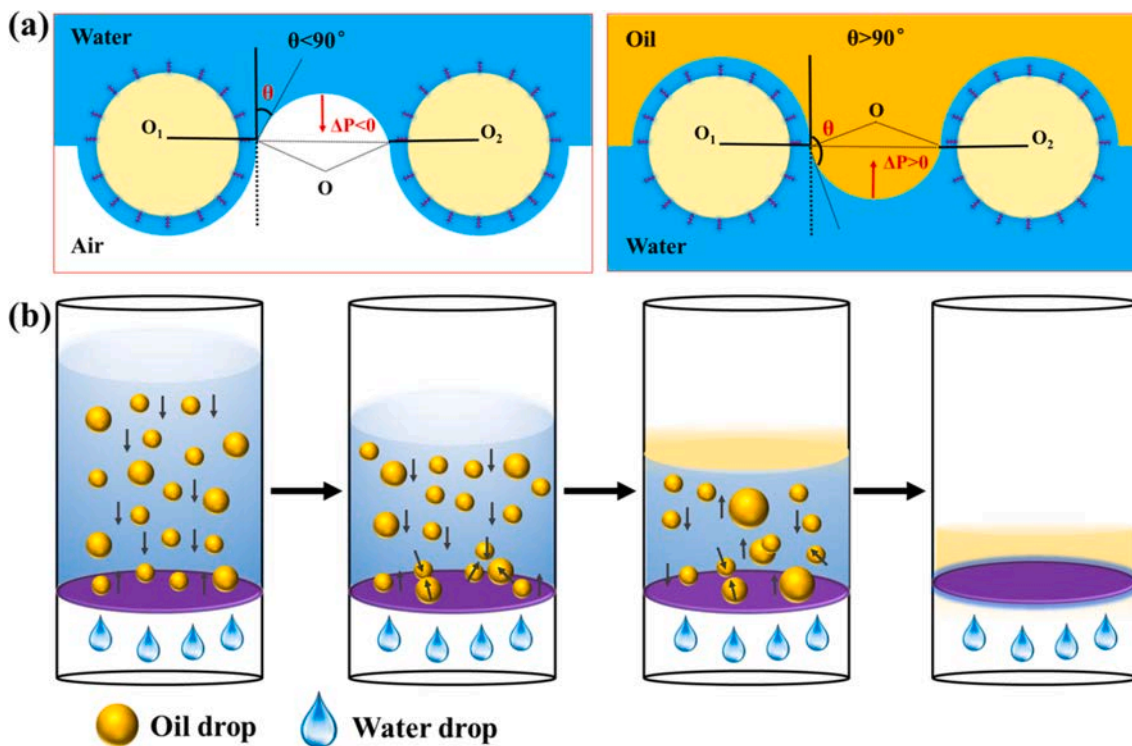


Fig. 8. Schematic illustration of (a) the membrane being wetted by water and oil and (b) possible mechanism of oil-in-water emulsion separation of the NF@CM@BM heterojunction membrane.

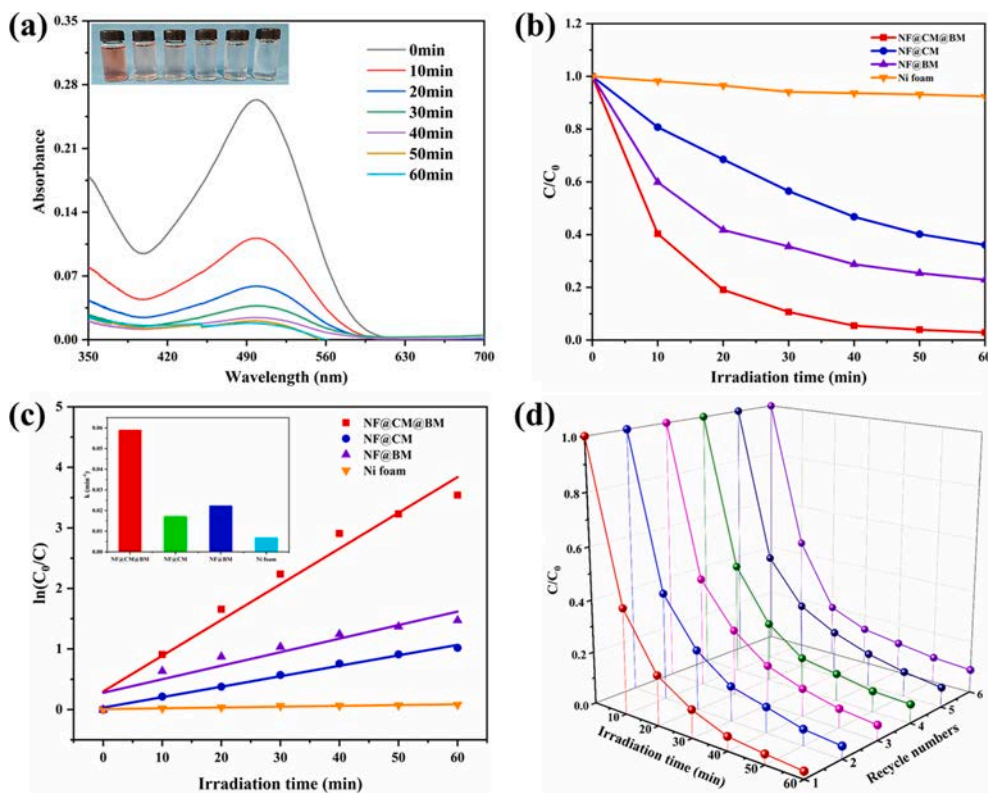


Fig. 9. (a) The absorbance curve of CR solution during the photodegradation process. (b) Photocatalytic degradation of CR solution using pristine Ni foam, NF@CM, NF@BM and NF@CM@BM. (c) The degradation rate constants of different samples. (d) Photocatalytic recycle experiment of the NF@CM@BM heterojunction membrane.

of the visible spectrum, not limited to the use of the ultraviolet light in the solar spectrum. In addition, the as-prepared membrane exhibited good reusability. After 6 cycles (Fig. 9d), the value of C/C_0 rose slightly and the photocatalytic efficiency was stable above 90%, indicating that it possessed great potential in practical applications.

In order to investigate the separation properties of photogenerated charge carriers in samples of NF@CM, NF@BM and NF@CM@BM, the electrochemical impedance spectra (EIS) experiment was carried out in a standard three-electrode system with CHI 760E electrochemical workstation. The as prepared samples ($1 \times 1.5 \text{ cm}^2$), graphite electrode and saturated calomel electrode were taken as work electrode, counter electrode and reference electrode, respectively. Meanwhile, 1 M Na_2SO_4 aqueous solution was served as electrolyte. In the test, the applied bias voltage was set to open circuit voltage, and the EIS was recorded in the frequency range of 10^6 Hz to 0.01 Hz with 5 mV AC amplitude. Generally, the smaller the semicircle diameter in EIS Nyquist plot, the lower the charge transfer resistance and the better the charge transfer ability [52]. It could be observed from Fig. 10a that compared with NF@CM and NF@BM, the NF@CM@BM heterojunction membrane possessed the smallest arc radius of the Nyquist plots, indicating that NF@CM@BM possessed the lowest resistance and the highest separation efficiency of electron-hole pairs.

In addition, the active species trapping experiments were performed to further investigate the photocatalytic mechanism of NF@CM@BM heterojunction membrane for CR solution. During the photodegradation processes, the scavengers of p-benzoquinone (BQ), isopropanol (IPA) and ethylenediamine tetraacetic acid (EDTA) with the concentration of 1 mM were added into the CR solution separately to quench major active

species superoxide radicals ($\cdot\text{O}_2^-$), hydroxyl radicals ($\cdot\text{OH}$) and electron holes (h^+), respectively. As shown in Fig. 10b, after introducing BQ or EDTA into the solution, the degradation efficiency of NF@CM@BM membrane to CR dropped significantly from 97.1% to 38.42% and 54.60%, indicating the dominant role of $\cdot\text{O}_2^-$ and h^+ in the photocatalytic process. However, the addition of IPA caused a slight decrease in the degradation efficiency of the CR solution, implying that the photocatalytic activity of NF@CM@BM membrane was slightly inhibited and the relative lower contribution of $\cdot\text{OH}$ in the photocatalytic process. To further verify the active species of $\cdot\text{O}_2^-$ and $\cdot\text{OH}$ produced during the degradation process of Congo red under visible light irradiation, the electron spin resonance (ESR) was performed and the 5,5-dimethyl-1-pyrroline-N-oxide (DMPO) was taken as the capture agent. From the obtained results of ESR in Fig. 10c and Fig. 10d, it could be observed that there were no characteristic ESR signals of $\cdot\text{O}_2^-$ and $\cdot\text{OH}$ under dark condition. However, after 30 min of visible light exposure, the characteristic peaks with relative intensities of 1:1:1:1 and 1:2:2:1 corresponding to DMPO- $\cdot\text{O}_2^-$ and DMPO- $\cdot\text{OH}$ were obtained, which indicated the generation of $\cdot\text{O}_2^-$ and $\cdot\text{OH}$ under visible light irradiation. Meanwhile, combined with the active species trapping experiments, it could be fully proved that the active species were produced and participate in the photocatalytic degradation reaction.

Based on the aforementioned analysis, a possible photocatalytic mechanism for the degradation of CR by NF@CM@BM p-n heterojunction membrane was proposed (Fig. 11). Due to the construction of $\text{CoMoO}_4/\text{Bi}_2\text{MoO}_6$ heterojunction nanoarrays between p-type CoMoO_4 and n-type Bi_2MoO_6 on Ni foam, the absorption range and absorption intensity of NF@CM@BM heterojunction membrane to visible light are

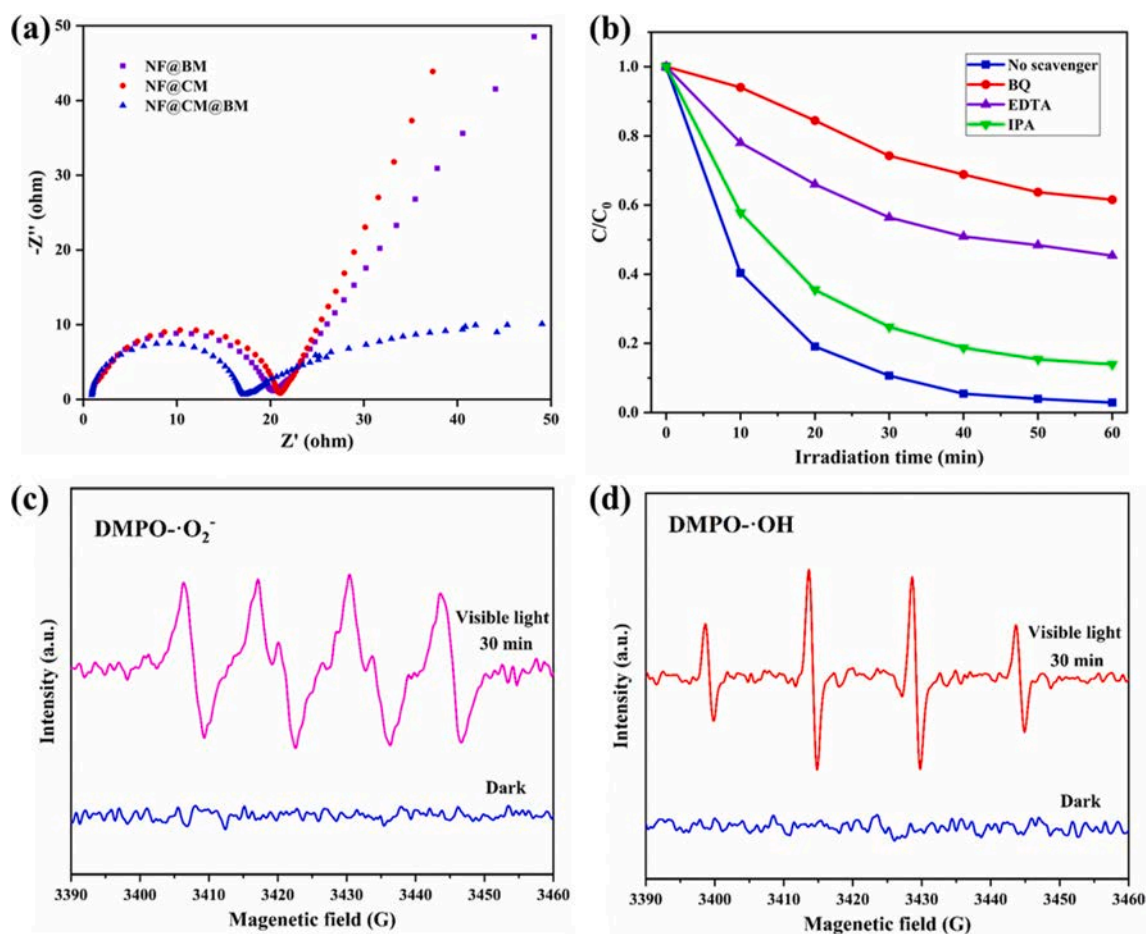


Fig. 10. (a) EIS Nyquist impedance plots of NF@CM, NF@BM and NF@CM@BM. (b) Photocatalytic degradation of CR solution with NF@CM@BM in the presence of various scavengers under visible light. (c) The ESR spectra of DMPO- $\cdot\text{O}_2^-$ and (d) DMPO- $\cdot\text{OH}$ in the presence of NF@CM@BM under dark and visible light irradiation, respectively.

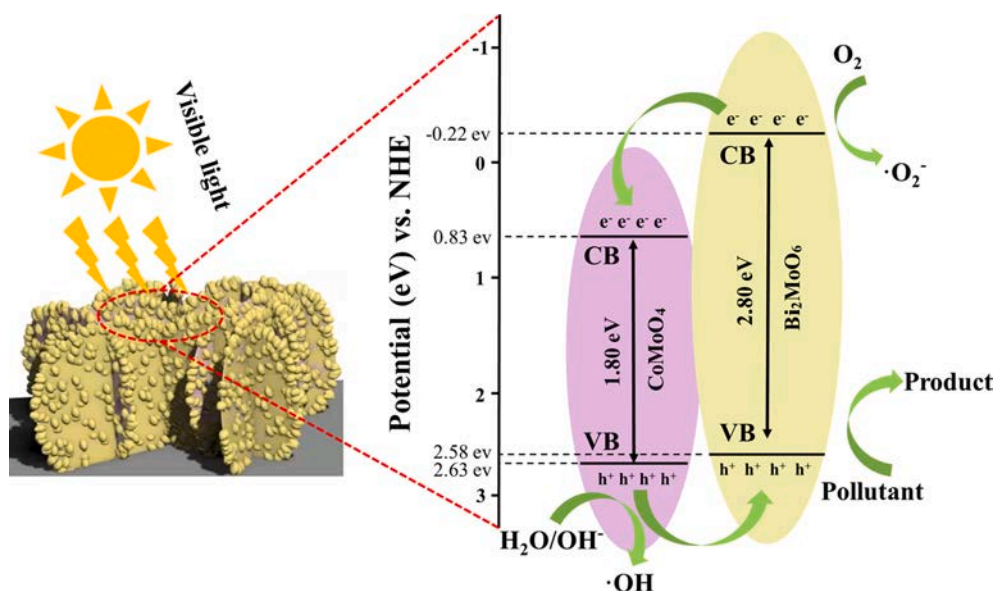
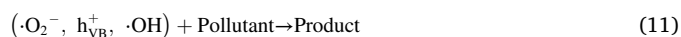


Fig. 11. Schematic illustrating of possible mechanism of photocatalytic degradation of the NF@CM@BM.

all increased, which makes it to generate more photogenerated electron-hole pairs [53]. According to previous reports, the valence band (VB) of CoMoO₄ and Bi₂MoO₆ are 2.63 eV and 2.58 eV, respectively [27,46]. Therefore, combined with the results of UV-vis DRS, the conduction band (CB) potential of corresponding samples are calculated to be 0.83 eV and -0.22 eV with the equation of $E_{VB} = E_{CB} + E_g$. After anchoring the irregular Bi₂MoO₆ nanoparticles on the CoMoO₄ nanosheets, due to their different Fermi energy levels, the energy band position will change and an internal electric field is formed in the interface at the same time [54,55]. Under visible light irradiation, the NF@CM@BM heterojunction membrane with the appropriate band gap can be excited to generate photogenerated electrons and holes (Eq. (7)). Compared with CoMoO₄, due to the more negative VB potential and more positive CB potential of Bi₂MoO₆, photogenerated electrons will easily transfer from the CB of Bi₂MoO₆ to CoMoO₄, while the corresponding holes transfer from the VB of CoMoO₄ to Bi₂MoO₆, thus effectively suppressing the recombination of photogenerated electrons and holes [34]. Meanwhile, the CB potential of Bi₂MoO₆ (-0.22 eV) is more negative than the standard redox potential of O₂/·O₂⁻ (-0.046 eV vs NHE) [56], indicating that the dissolved O₂ can be reduced to ·O₂⁻ by accumulated electrons in the CB of Bi₂MoO₆ (Eq. (8)). The holes generated in the VB of CoMoO₄ can either oxidize H₂O/OH⁻ to ·OH due to the higher potential (2.63 eV) than H₂O/·OH (+1.99 eV vs NHE) (Eq. (9)) [57] or react with pollutant directly (Eq. (10)). In summary, ·O₂⁻, holes, ·OH are the mainly active species for the photocatalytic degradation of CR solution (Eq. (11)), which has been confirmed by active species trapping experiments. Therefore, the excellent photocatalytic performance of the NF@CM@BM membrane is attributed to the formation of CoMoO₄@-Bi₂MoO₆ p-n heterojunction.



To further understand the degradation process, the liquid chromatography-mass spectrometry (LC-MS) measurements were carried out to analyze possible intermediate products of CR catalyzed with

NF@CM@BM under visible light irradiation and the products were identified by interpretation of their mass spectra data presenting their molecule ion peaks with respect to m/z . CR was a sulfonated compound with negative pseudo-molecular ion at m/z value of 650. From the LC-MS results in Fig. S8, it could be observed that main peaks were located at the m/z value of 520.91, 452.92, 384.93, 316.95, 248.96, 180.97, 112.98, 96.96, 68.99 and 61.98, which indicated that the unsaturated bonds of CR were attacked by oxidizing radicals and cleaved into various species. According to the results of m/z value, possible products during the photocatalytic degradation of CR in the presence of NF@CM@BM were analyzed. Based on this and relevant reports [58,59], a possible degradation pathway was proposed and presented in Fig. S9.

3.5. Recyclability and stability of NF@CM@BM membrane

Generally, in the process of oil-in-water emulsion separation, recyclability and stability are two key factors to evaluate whether the membrane can effectively separate oil-water emulsions for a long-term. The recyclability of the NF@CM@BM heterojunction membrane was evaluated with petroleum ether-in-water emulsion. As shown in Fig. 12a, as the separation cycles increased, there was no significant change of the separation efficiency, and the separation efficiency maintained higher than 99%. After repeated for 20 cycles, although the flux is slightly reduced compared with the initial filtrated flux, it still remains at a high level of 1208.10 L m⁻² h⁻¹, indicating the attractive recyclability of the NF@CM@BM membrane, which was attributed to its strong anti-oil-adhesion ability. In addition, the verification test of stability of NF@CM@BM heterojunction membrane was conducted by placing the membrane in an ultrasonic cleaning machine with powder of 50 W. As presented in Fig. 12b, the underwater OCA hardly changed until after 40 min of ultrasonic treatment. Subsequently, with the increase of the ultrasound time, Underwater OCA decreased slightly, but still greater than 150°. Furthermore, the the as-prepared membrane remained high separation efficiency of 99.09% for petroleum ether-in-water emulsion after 60 min of vibration. Additionally, it could be clearly observed from the SEM image (shown in Fig. S10) that the microstructure of hierarchical CoMoO₄@Bi₂MoO₆ core-shell nanoarrays relatively intact. These results indicated that the NF@CM@BM membrane possessed favorable stability, implying its promising in the practical application.

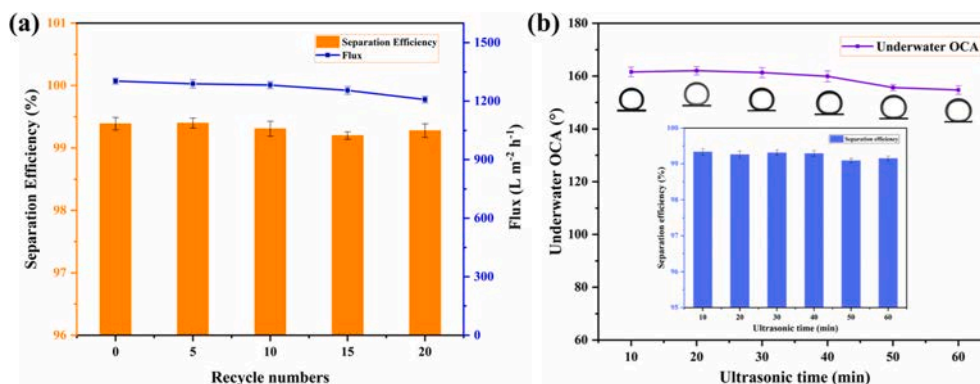


Fig. 12. (a) Separation efficiency and permeation flux of petroleum ether-in-water emulsion for repeated use. (b) The separation efficiency and underwater OCA after different ultrasonic time.

4. Conclusion

In summary, NF@CM@BM membrane with attractive photocatalytic performance was prepared via a facile two-step hydrothermal process combined with calcination methods, and the growth process of Bi₂MoO₆ on CoMoO₄ nanosheets was also investigated. Due to the rough hierarchical structure and the composition of hydrophilic molybdate, the as-prepared membrane exhibited favorable superhydrophilicity and underwater superoleophobicity with underwater OCA of 162.5°, so it could separate oil-in-water emulsions completely driven by gravity, with high separation efficiency of 99.67% and flux of 1449.12 L m⁻² h⁻¹. In addition, the formation of p-n heterojunction between CoMoO₄ and Bi₂MoO₆ significantly improved its photodegradation ability to CR by suppressing the recombination of photogenerated electron-hole pairs and enhancing the response to visible light. More importantly, the heterojunction membrane exhibited favorable recyclability and stability no matter in the separation of oil-water emulsions or in the degradation of water-soluble dyes. Therefore, it is believed that this work offers a creative strategy for the synergistic application of photocatalysis and special wettability in the wastewater remediation.

CRedit authorship contribution statement

Jingshuai Li: Conceptualization, Methodology, Software, Validation, Formal analysis, Investigation, Resources, Data curation, Writing – original draft, Writing – review & editing, Visualization, Supervision, Project administration. **Yongli Sun:** Validation, Supervision, Project administration, Funding acquisition, Project administration. **Luhong Zhang:** Validation, Supervision, Project administration, Funding acquisition, Project administration. **Xiaoming Xiao:** Validation, Supervision, Project administration, Funding acquisition, Project administration. **Na Yang:** Validation, Writing – review & editing, Supervision. **Longfei Zhang:** Software, Validation, Writing – review & editing. **Xiaodong Yang:** Software, Validation, Writing – review & editing. **Feifei Peng:** Supervision. **Bin Jiang:** Validation, Supervision, Project administration, Funding acquisition, Project administration.

Declaration of Competing Interest

The authors declare that they have no known competing financial interests or personal relationships that could have appeared to influence the work reported in this paper.

Acknowledgements

We are grateful for the financial support from National Key R&D Program of China (No. 2016YFC0400406)

Appendix A. Supplementary data

Supplementary data to this article can be found online at <https://doi.org/10.1016/j.seppur.2021.119568>.

References

- [1] A. Ahmad, A. Kusumastuti, C. Derek, B. Ooi, Emulsion liquid membrane for heavy metal removal: an overview on emulsion stabilization and destabilization, *Chem. Eng. J.* 171 (2011) 870–882.
- [2] Y.-P. An, J. Yang, H.-C. Yang, M.-B. Wu, Z.-K. Xu, Janus membranes with charged carbon nanotube coatings for deemulsification and separation of oil-in-water emulsions, *ACS Appl. Mater. Interfaces* 10 (2018) 9832–9840.
- [3] R.K. Gupta, G.J. Dunderdale, M.W. England, A. Hozumi, Oil/water separation techniques: a review of recent progresses and future directions, *J. Mater. Chem. A* 5 (2017) 16025–16058.
- [4] Z. Shi, W. Zhang, F. Zhang, X. Liu, D. Wang, J. Jin, L. Jiang, Ultrafast separation of emulsified oil/water mixtures by ultrathin free-standing single-walled carbon nanotube network films, *Adv. Mater.* 25 (17) (2013) 2422–2427.
- [5] M. Tao, L. Xue, F.u. Liu, L. Jiang, An intelligent superwetting PVDF membrane showing switchable transport performance for oil/water separation, *Adv. Mater.* 26 (18) (2014) 2943–2948.
- [6] E.N. Tummmons, J.W. Chew, A.G. Fane, V.V. Tarabara, Ultrafiltration of saline oil-in-water emulsions stabilized by an anionic surfactant: effect of surfactant concentration and divalent counterions, *J. Membr. Sci.* 537 (2017) 384–395.
- [7] Y. Jiang, H. Qi, X. Zhang, Novel method for separation and screening of lubricant-degrading microorganisms and bacterial biodegradation, *Chin. J. Chem. Eng.* 24 (3) (2016) 353–359.
- [8] W. Zhang, N. Liu, Y. Cao, X. Lin, Y. Liu, L. Feng, Superwetting porous materials for wastewater treatment: from immiscible oil/water mixture to emulsion separation, *ACS Appl. Mater. Interfaces* 4 (2017) 1600029.
- [9] W. Zheng, J. Huang, S. Li, M. Ge, L. Teng, Z. Chen, Y. Lai, Advanced materials with special wettability toward intelligent oily wastewater remediation, *ACS Appl. Mater. Interfaces* 13 (1) (2021) 67–87.
- [10] Y. Peng, Z. Guo, Recent advances in biomimetic thin membranes applied in emulsified oil/water separation, *J. Mater. Chem. A* 4 (41) (2016) 15749–15770.
- [11] M.M. Pendergast, E.M.V. Hoek, A review of water treatment membrane nanotechnologies, *Energy Environ. Sci.* 4 (6) (2011) 1946, <https://doi.org/10.1039/c0ee00541j>.
- [12] D. Rana, T. Matsuura, Surface modifications for antifouling membranes, *Chem. Rev.* 110 (4) (2010) 2448–2471.
- [13] M.A. Shannon, P.W. Bohn, M. Elimelech, J.G. Georgiadis, B.J. Mariñas, A. M. Mayes, in: *Nanoscience and Technology: A Collection of Reviews from Nature Journals*, Co-Published with Macmillan Publishers Ltd, UK, 2009, pp. 337–346, https://doi.org/10.1142/9789814287005_0035.
- [14] L. Qiu, Y. Sun, Z. Guo, Designing novel superwetting surfaces for high-efficiency oil-water separation: design principles, opportunities, trends and challenges, *J. Mater. Chem. A* 8 (2020) 16831–16853.
- [15] Y. Yin, L. Zhu, X. Chang, J. Xue, S. Yu, X. Li, Q. Xue, Bioinspired anti-oil-fouling hierarchical structured membranes decorated with urchin-like α-FeOOH particles for efficient oil/water mixture and crude oil-in-water emulsion separation, *ACS Appl. Mater. Interfaces* 12 (45) (2020) 50962–50970.
- [16] H. Zhang, Z. Wang, Y. Shen, P. Mu, Q. Wang, J. Li, Ultrathin 2D Ti₃C₂T_x MXene membrane for effective separation of oil-in-water emulsions in acidic, alkaline, and salty environment, *J. Colloid Interface Sci.* 561 (2020) 861–869.
- [17] S. Yan, Y. Li, F. Xie, J. Wu, X. Jia, J. Yang, H. Song, Z. Zhang, Environmentally safe and porous MS@TiO₂@PPy monoliths with superior visible-light photocatalytic properties for rapid oil-water separation and water purification, *ACS Sustain. Chem. Eng.* 8 (13) (2020) 5347–5359.
- [18] B. Xu, X. Wang, Y. Huang, J. Liu, D. Wang, S. Feng, X. Huang, H. Wang, Electrospinning preparation of PAN/TiO₂/PANI hybrid fiber membrane with

- highly selective adsorption and photocatalytic regeneration properties, *Chem. Eng. J.* 399 (2020), 125749.
- [19] C. Xu, K. Yan, P. Wang, X. Zhou, T. Zhang, Y. Fu, Q. Yan, CuBi_2O_4 and rGO co-modified 3D hierarchical flower-like $\text{Bi}_5\text{O}_7\text{I}$ nanoflakes as Z-scheme heterojunction for enhanced photocatalytic performance, *Sep. Purif. Technol.* 257 (2021), 117935.
- [20] X. Jiang, Z. Zhang, M. Sun, W. Liu, J. Huang, H. Xu, Self-assembly of highly-dispersed phosphotungstic acid clusters onto graphitic carbon nitride nanosheets as fascinating molecular-scale Z-scheme heterojunctions for photocatalytic solar-to-fuels conversion, *Appl. Catal. B-Environ.* 281 (2021), 119473.
- [21] C. Huang, S. Zou, Y.e. Liu, S. Zhang, Q. Jiang, T. Zhou, S. Xin, J. Hu, Surface reconstruction-associated partially amorphized bismuth oxychloride for boosted photocatalytic water oxidation, *ACS Appl. Mater. Interfaces* 13 (4) (2021) 5088–5098.
- [22] X. Wu, C.Y. Toe, C. Su, Y.H. Ng, R. Amal, J. Scott, Preparation of Bi-based photocatalysts in the form of powdered particles and thin films: a review, *J. Mater. Chem. A* 8 (31) (2020) 15302–15318.
- [23] W. Shi, M. Li, X. Huang, H. Ren, F. Guo, Y. Tang, C. Lu, Construction of $\text{CuBi}_2\text{O}_4/\text{Bi}_2\text{MoO}_6$ p-n heterojunction with nanosheets-on-microrods structure for improved photocatalytic activity towards broad-spectrum antibiotics degradation, *Chem. Eng. J.* 394 (2020), 125009.
- [24] W. Dai, W. Xiong, J. Yu, S. Zhang, B. Li, L. Yang, T. Wang, X. Luo, J. Zou, S. Luo, Reduced graphene oxide layer with Bi_2MoO_6 quantum dots in-situ grown on: a novel electron-rich interface for efficient CO_2 reduction, *ACS Appl. Mater. Interfaces* (2020).
- [25] H. Li, Z. Zheng, M. Liu, H. Jiang, D. Hu, X. Zhang, L. Xia, X. Geng, J. Lu, X. Cheng, Visible light photo-treatment of simulated wastewater activated by high-efficient photocatalyst: a novel heterojunction of Bi_2MoO_6 balls and Pd nanoskeletons, *Appl. Surf. Sci.* 510 (2020), 145468.
- [26] M. Li, D. Li, Z. Zhou, P. Wang, X. Mi, Y. Xia, H. Wang, S. Zhan, Y. Li, L. Li, Plasmonic Ag as electron-transfer mediators in $\text{Bi}_2\text{MoO}_6/\text{Ag-AgCl}$ for efficient photocatalytic inactivation of bacteria, *Chem. Eng. J.* 382 (2020), 122762.
- [27] K. Zhao, Z. Zhang, Y. Feng, S. Lin, H. Li, X. Gao, Surface oxygen vacancy modified $\text{Bi}_2\text{MoO}_6/\text{ML-88B}$ (Fe) heterostructure with enhanced spatial charge separation at the bulk&interface, *Appl. Catal. B-Environ.* 268 (2020), 118740.
- [28] H. Zhang, H.e. Bian, H. Zhang, B. Xu, C. Wang, L. Zhang, D. Li, F. Wang, Magnetic separable $\text{Bi}_2\text{Fe}_4\text{O}_9/\text{Bi}_2\text{MoO}_6$ heterojunctions in Z-scheme with enhanced visible-light photocatalytic activity for organic pollutant degradation, *Catal. Lett.* 150 (9) (2020) 2464–2473.
- [29] F. Fu, H. Shen, X. Sun, W. Xue, A. Shoneye, J. Ma, L. Luo, D. Wang, J. Wang, J. Tang, Synergistic effect of surface oxygen vacancies and interfacial charge transfer on Fe (III)/ Bi_2MoO_6 for efficient photocatalysis, *Appl. Catal. B-Environ.* 247 (2019) 150–162.
- [30] Y. Ma, Y. Jia, Y. Lin, W. Shi, Hierarchical $\text{Ag}/\text{Bi}_2\text{MoO}_6$ hollow nanoboxes with high photocatalytic performance, *Dalton Trans.* 48 (32) (2019) 12009–12012.
- [31] X. Xu, X. Ding, X. Yang, P. Wang, S. Li, Z. Lu, H. Chen, Oxygen vacancy boosted photocatalytic decomposition of ciprofloxacin over Bi_2MoO_6 : Oxygen vacancy engineering, biotoxicity evaluation and mechanism study, *J. Hazard. Mater.* 364 (2019) 691–699.
- [32] J. Hu, J. Li, J. Cui, W. An, L. Liu, Y. Liang, W. Cui, Surface oxygen vacancies enriched $\text{FeOOH}/\text{Bi}_2\text{MoO}_6$ photocatalysis-fenton synergy degradation of organic pollutants, *J. Hazard. Mater.* 384 (2020), 121399.
- [33] K. Jing, W. Ma, Y. Ren, J. Xiong, B. Guo, Y. Song, S. Liang, L. Wu, Hierarchical Bi_2MoO_6 spheres in situ assembled by monolayer nanosheets toward photocatalytic selective oxidation of benzyl alcohol, *Appl. Catal. B-Environ.* 243 (2019) 10–18.
- [34] X. Zou, Y. Dong, J. Ke, H. Ge, D. Chen, H. Sun, Y. Cui, Cobalt monoxide/tungsten trioxide p-n heterojunction boosting charge separation for efficient visible-light-driven gaseous toluene degradation, *Appl. Catal. B-Environ.* 400 (2020), 125919.
- [35] C. Zhang, W. Fei, H. Wang, N. Li, D. Chen, Q. Xu, H. Li, J. He, J. Lu, pn Heterojunction of BiOI/ZnO nanorod arrays for piezo-photocatalytic degradation of bisphenol A in water, *J. Hazard. Mater.* 399 (2020), 123109.
- [36] Y. Sun, J. Li, L. Zhang, B. Jiang, X. Yang, N. Yang, F. Peng, M. Xu, X. Xiao, Dual-functional mesh with Zn-Ni-Co LDHs@ NiMoO_4 heterojunction nanoarrays for highly efficient oil/water separation and photocatalytic degradation, *Sep. Purif. Technol.* 259 (2021), 118116.
- [37] W. Xiao, J.S. Chen, C.M. Li, R. Xu, X.W. Lou, Synthesis, characterization, and lithium storage capability of AMoO_4 (A = Ni, Co) nanorods, *Chem. Mat.* 22 (3) (2010) 746–754.
- [38] G. Tian, Y. Chen, J. Zhou, C. Tian, R. Li, C. Wang, H. Fu, In situ growth of Bi_2MoO_6 on reduced graphene oxide nanosheets for improved visible-light photocatalytic activity, *CrystEngComm* 16 (5) (2014) 842–849.
- [39] Y. Shen, Z. Li, Z. Cui, K.e. Zhang, R. Zou, F. Yang, K. Xu, Boosting the interface reaction activity and kinetics of cobalt molybdate by phosphating treatment for aqueous zinc-ion batteries with high energy density and long cycle life, *J. Mater. Chem. A* 8 (40) (2020) 21044–21052.
- [40] D. Yu, Z. Zhang, Y. Teng, X. Zhao, X. Liu, Controllable synthesis of cobalt molybdate nanoarrays on nickel foam as the advanced electrodes of alkaline battery-supercapacitor hybrid devices, *J. Alloy. Compd.* 835 (2020), 155244.
- [41] J. Tian, P. Hao, N. Wei, H. Cui, H. Liu, 3D Bi_2MoO_6 nanosheet/ TiO_2 nanobelt heterostructure: enhanced photocatalytic activities and photoelectrochemistry performance, *ACS Catal.* 5 (2015) 4530–4536.
- [42] J. Li, Y. Zhao, M. Xia, H. An, H. Bai, J. Wei, B. Yang, G. Yang, Highly efficient charge transfer at 2D/2D layered P- $\text{La}_2\text{Ti}_2\text{O}_7/\text{Bi}_2\text{WO}_6$ contact heterojunctions for upgraded visible-light-driven photocatalysis, *Appl. Catal. B-Environ.* 261 (2020), 118244.
- [43] M. Xia, X. Yan, H. Li, N. Wells, G. Yang, Well-designed efficient charge separation in 2D/2D N doped $\text{La}_2\text{Ti}_2\text{O}_7/\text{ZnIn}_2\text{S}_4$ heterojunction through band structure/morphology regulation synergistic effect, *Nano Energy* 78 (2020), 105401.
- [44] M. Pirhashemi, A. Habibi-Yangjeh, Facile fabrication of novel $\text{ZnO}/\text{CoMoO}_4$ nanocomposites: Highly efficient visible-light-responsive photocatalysts in degradations of different contaminants, *Photochem. Photobiol.* 363 (2018) 31–43.
- [45] Z. Gao, H. Yang, Y. Cao, Q. Wu, L. Kang, J. Mao, J. Wu, Complete mineralization of a humic acid by $\text{SO}_4^{\cdot-}$ generated on $\text{CoMoO}_4/\text{gC}_3\text{N}_4$ under visible-light irradiation, *Nanotechnology* 30 (2019), 255704.
- [46] X. Zhang, S. Lou, Y. Zeng, Facile fabrication of a novel visible light active $\text{g-C}_3\text{N}_4\text{-CoMoO}_4$ heterojunction with largely improved photocatalytic performance, *Mater. Lett.* 281 (2020), 128661.
- [47] N. Zhang, N. Yang, L. Zhang, B. Jiang, Y. Sun, J. Ma, K. Cheng, F. Peng, Facile hydrophilic modification of PVDF membrane with Ag/EGCG decorated micro/nanostructural surface for efficient oil-in-water emulsion separation, *Chem. Eng. J.* 402 (2020), 126200.
- [48] J. Ge, D. Zong, Q. Jin, J. Yu, B. Ding, Biomimetic and superwetable nanofibrous skins for highly efficient separation of oil-in-water emulsions, *Adv. Funct. Mater.* 28 (2018) 1705051.
- [49] J. Zuo, Z. Liu, C. Zhou, Y. Zhou, X. Wen, S. Xu, J. Cheng, P. Pi, A durable superwetting clusters-inlayed mesh with high efficiency and flux for emulsion separation, *J. Hazard. Mater.* 403 (2021), 123620.
- [50] B. Jiang, Z. Chen, H. Dou, Y. Sun, H. Zhang, Z.Q. Gong, L. Zhang, Superhydrophilic and underwater superoleophobic Ti foam with fluorinated hierarchical flower-like TiO_2 nanostructures for effective oil-in-water emulsion separation, *Appl. Surf. Sci.* 456 (2018) 114–123.
- [51] S. Gao, J. Sun, P. Liu, F. Zhang, W. Zhang, S. Yuan, J. Li, J. Jin, A robust polyionized hydrogel with an unprecedented underwater anti-crude-oil-adhesion property, *Adv. Mater.* 28 (26) (2016) 5307–5314.
- [52] L. Tian, S. Min, F. Wang, Integrating noble-metal-free metallic vanadium carbide cocatalyst with CdS for efficient visible-light-driven photocatalytic H_2 evolution, *Appl. Catal. B-Environ.* 259 (2019), 118029.
- [53] Y.-X. Tan, Z.-M. Chai, B.-H. Wang, S. Tian, X.-X. Deng, Z.-J. Bai, L. Chen, S. Shen, J.-K. Guo, M.-Q. Cai, Boosted photocatalytic oxidation of toluene into benzaldehyde on $\text{CdIn}_2\text{S}_4\text{-CdS}$: synergetic effect of compact heterojunction and S-vacancy, *ACS Catal.* 11 (2021) 2492–2503.
- [54] L.u. Wang, R. Wang, Y. Zhou, Q. Shen, JinHua Ye, C. Wu, Z. Zou, Three-dimensional $\text{Bi}_2\text{MoO}_6/\text{TiO}_2$ array heterojunction photoanode modified with cobalt phosphate cocatalyst for high-efficient photoelectrochemical water oxidation, *Catal. Today* 335 (2019) 262–268.
- [55] R. He, D. Xu, B. Cheng, J. Yu, W. Ho, Review on nanoscale Bi-based photocatalysts, *Nanoscale Horiz.* 3 (5) (2018) 464–504.
- [56] L. Ye, J. Chen, L. Tian, J. Liu, T. Peng, K. Deng, L. Zan, BiOI thin film via chemical vapor transport: photocatalytic activity, durability, selectivity and mechanism, *Appl. Catal. B-Environ.* 130 (2013) 1–7.
- [57] H. Wang, S.i. Chen, Z. Wang, Y.i. Zhou, Z. Wu, A novel hybrid $\text{Bi}_2\text{MoO}_6\text{-MnO}_2$ catalysts with the superior plasma induced pseudo photocatalytic-catalytic performance for ethyl acetate degradation, *Appl. Catal. B-Environ.* 254 (2019) 339–350.
- [58] N. Güy, S. Çakar, M. Özacar, Comparison of palladium/zinc oxide photocatalysts prepared by different palladium doping methods for Congo red degradation, *J. Colloid Interface Sci.* 466 (2016) 128–137.
- [59] U. Arellano, J.A. Wang, L.F. Chen, M. Asomoza, A. Guzmán, S. Solís, A. Estrella, S. Cipagauta, L.E. Noreña, Transition metal oxides dispersed on Ti-MCM-41 hybrid core-shell catalysts for the photocatalytic degradation of Congo red colorant, *Catal. Today* 349 (2020) 128–140.